

Nova indirect drive Rayleigh–Taylor experiments with beryllium

M. M. Marinak, S. G. Glendinning, R. J. Wallace, B. A. Remington, S. V. Weber,
S. W. Haan, and G. W. Collins

Lawrence Livermore National Laboratory, Livermore, California 94551

(Received 5 March 2002; accepted 22 May 2002)

The growth due to the Rayleigh–Taylor (RT) instability of single-wavelength surface perturbations on planar foils of copper-doped beryllium [BeCu] was measured. These foils were accelerated by x-ray ablation, with a shaped drive designed to produce ~ 1.5 ns of uniform acceleration. A range of wavelengths ($\lambda = 30\text{--}70\ \mu\text{m}$) was used with initial amplitudes $\eta_0/\lambda = 0.03\text{--}0.04$. Tabulated opacities from detailed atomic physics models, HOPE [J. Quant. Spectros. Radiat. Transf. **43**, 381 (1990)], OPAL [Astrophys. J. **397**, 717 (1992)] and super transition array (STA) [Phys. Rev. A **40**, 3183 (1989)] were employed in simulations. Other ingredients which can affect modeling, such as changes in the equation of state and the radiation drive spectrum, were also examined. This calculational model agrees with the Nova single wavelength RT perturbation growth data for the BeCu. No adjustments to the modelling parameters were necessary. © 2002 American Institute of Physics. [DOI: 10.1063/1.1494821]

I. INTRODUCTION

In the design of an inertial confinement fusion (ICF) ignition capsule the choice of the ablator material has far ranging consequences. Several properties of the ablator material are tied to the requirements for energy, power and pulse length from the driver. These include the density of the ablator, its specific heat and its opacity. The minimum thickness of the ablator, which strongly relates to requirements on the driver, is limited by the growth of hydrodynamic instabilities in the ablator, which depend upon ablator properties. Methods available for filling a cryogenic capsule differ among the ablator materials, as do requirements for temperature uniformity in the hohlraum. The National Ignition Facility (NIF) is a 192 beam frequency tripled ($\lambda = 0.35\ \mu\text{m}$) Nd:glass laser system, under construction, capable of generating shaped pulses delivering 1.8 MJ at a peak power of 500 TW. Assuming the NIF laser performs according to specifications, detailed computer simulations^{1–8} have identified a variety of indirectly driven target designs which can achieve ignition. These achieve ignition over energies ranging from 0.9 to 1.8 MJ with the range of peak drive temperatures varying from 250 to 400 eV. These capsules utilize a variety of ablator materials including different plastics, copper-doped beryllium and boron carbide (B_4C). Each of these materials brings specific advantages for the particular capsule design.

Capsule designs with beryllium ablators have been considered for the National Ignition Facility laser from its inception.^{1,9} The advantages of beryllium were discussed in detail by Wilson.⁷ These include lower sensitivity to ice surface roughness.^{7,8} Beryllium has higher thermal conductivity than plastic, reducing requirements for temperature uniformity in the hohlraum. Beryllium's lower opacity enables it to absorb more energy from the hohlraum. The lower specific heat of beryllium means that for fixed temperature and de-

posited energy more beryllium is ablated, resulting in greater ablative stabilization of Rayleigh–Taylor (RT) growth. Its higher density allows for a thinner ablator for a given mass, thus enabling a shorter laser pulse length for the first shock to traverse it.

The opaqueness of Be is a disadvantage because it makes difficult the measurement of the inner ice surface roughness. Also heating of the ice surface to reduce roughness is not possible with metallic Be. The grain structure of beryllium could help seed instability growth. Compared with plastic, there is less fabrication experience with Be in Nova experiments.

In the capsule designs copper dopant is added to the Be, to give it the extra opacity needed to inhibit radiation preheat of the fuel and to adjust the penetration of the radiation ablation front into the ablator. Copper was chosen as the dopant for Be because it has the highest solubility of any element. A variety of methods for producing doped Be ablator capsules are being developed. In one approach the BeCu is sputter deposited onto a mandrel.¹⁰ In another hollow BeCu hemispheres are brazed together and machined into a sphere.¹¹ Beryllium fabrication through a chemical vapor deposition process is also under research.¹²

We present here experiments performed on the Nova laser which measured RT growth of perturbations on indirectly driven planar foils of sputtered BeCu. Planar geometry allows easier diagnosis of perturbations than the spherical geometry of an imploding shell. Our previous experimental studies of hydrodynamic instabilities in planar geometry^{13–18} have used doped plastic and fluoro-silicone foils to study a broad variety of effects, including single and multimode saturation and mode coupling. The present experiments investigate the hydrodynamic stability, in the linear and non-linear regime, of foils having a composition similar to the BeCu ablator in the NIF ignition capsule designs.

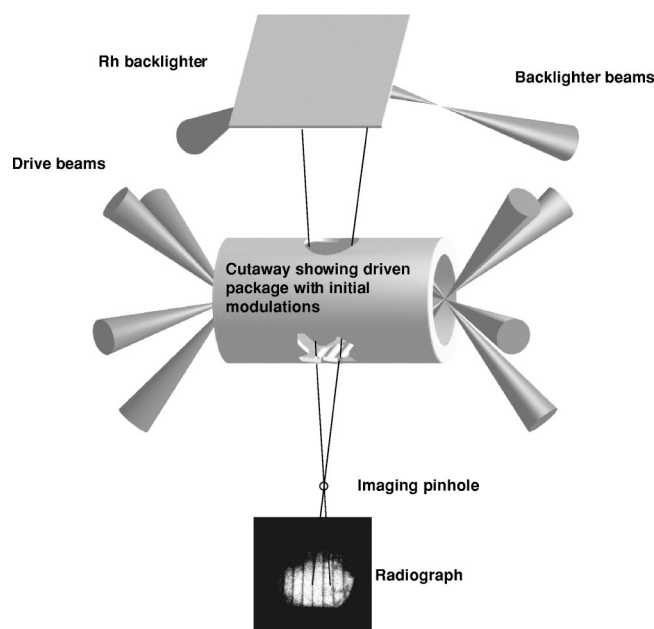


FIG. 1. Schematic of the geometry for experiments with face on radiography.

II. EXPERIMENT

Figure 1 illustrates the experimental geometry. Surface perturbations are molded onto one side of a BeCu foil 42–51 μm thick, $\rho = 2.1 \text{ g/cm}^3$, which is mounted across a 750 μm diameter hole in the wall of a 3000 μm long, 1000 μm diameter gold cylindrical hohlraum with the perturbations facing inward. The foil is illuminated from the back by a 600 μm diameter source of x rays created by irradiating a disk of rhodium with the Nova beams¹⁹ in a 2 ns square pulse. Perturbations on the foil modulate the transmitted backlighter flux according to

$$I(x, y, t) = I_0(x, y, t) e^{-|\kappa p| dz},$$

where κ is the opacity. Measurements of the transmitted backlighter intensity determine modulation of optical depth and therefore the amplitude of the areal density perturbation. A copper concentration of 3.3–3.9 % was used to make the foil sufficiently opaque to the backlighter to measure the perturbations. This is higher than for the NIF ignition capsule designs, which use 0.9% copper. Simulations indicate the higher Cu concentration results in a reduced ablator density gradient scale length, but does not dramatically change the ablator characteristics. The flexible x-ray pinhole imager (FXI) was used to obtain gated images.²⁰ Its resolution for these experiments was characterized earlier.¹⁷

Eight $\lambda = 0.351 \mu\text{m}$, 2.5 KJ shaped Nova beams irradiate the hohlraum with a low intensity $\sim 10 \text{ ns}$ foot followed by a rapid increase to peak power which is maintained during the interval 2.5–4.4 ns, with the ratio of peak to foot laser power being ~ 5 , shown in Fig. 2. This x-ray drive, which has been measured with the Dante x-ray diode array,²¹ creates a period of nearly uniform acceleration lasting $\sim 1.5 \text{ ns}$. This drive spectrum employed in the simulations was obtained from a Lasnex²² gold hohlraum simulation, with the amplitude renormalized to match the Dante radia-

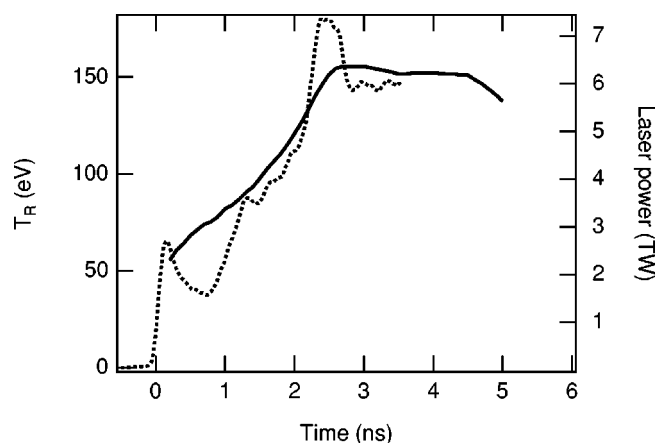


FIG. 2. Time history of the laser power (dashed curve) into the hohlraum and measured radiation drive history (solid curve).

tion intensity measurement, corrected for the albedo of the hohlraum wall. The spectrum shape varies with time through the laser pulse. A drive measurement was also obtained from a photoconducting diode array viewing from 23 degrees off the hohlraum axis through the laser entrance hole. For these shots an estimate based upon measurements of the power backscattered by laser plasma instabilities is $\leq 1\%$. This drive model reproduced well the measurement of the shock breakout trajectory through an aluminum wedge mounted on a hohlraum as viewed by a streaked UV imager.²³ It has also been used to model successfully the position of the back side of a Br-doped polystyrene foil.^{13–15,17}

Simulations of the BeCu foils were performed with Lasnex with three different methods for modelling the opacity of the BeCu mixture. One approach used the XSN opacity model.²⁴ We have also obtained multifrequency opacity tables for accurate atomic models. The HOPE model, which uses detailed configuration accounting with average atom wave functions,²⁵ was used to generate one table. A second table was generated by mixing results from the OPAL model for Be with results from the super transition array (STA) model for copper. The OPAL model²⁶ is based upon LS coupling and explicitly sums over individual atomic configurations, including term splitting. The OPAL model is most readily applied to lower Z material, while the STA model is more appropriate for higher Z materials. The STA model utilizes a JJ coupling scheme, and generates clusters of unresolved transition arrays.²⁷ We have not adjusted any parameters in these models.

Another modeling ingredient which affects the perturbation growth is the equation of state (EOS). We modeled the foils using the inline Quotidian Equations of State (QEOS) analytic model.²⁸ We also tried a Be table from a tabular EOS data base, with Thomas–Fermi scaling of the table EOS values for the composition difference of the material being modeled and that of the table. The effects of uncertainties for the drive model and the copper concentration have also been examined.

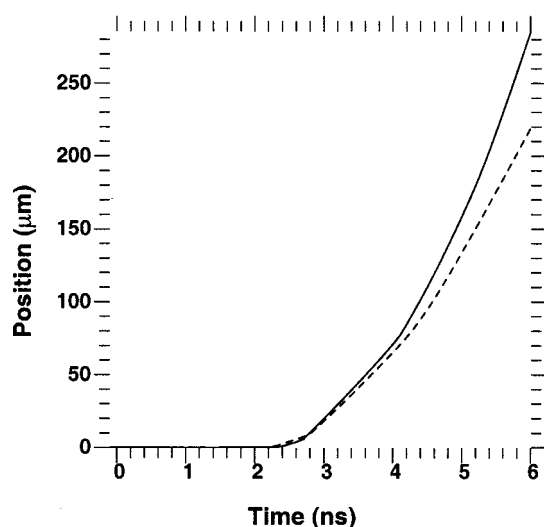


FIG. 3. Solid curve is apparent position of back of foil from 2D simulation of perturbed foil ($\lambda = 30 \mu\text{m}$, $\eta_0 = 2 \mu\text{m}$). Dashed curve is from simulation without perturbation.

A. Side on experiments

The foils used in the side-on experiments had sinusoidal perturbations with $\lambda = 30 \mu\text{m}$ and an amplitude of $2 \mu\text{m}$ peak to valley. Flat foils were unavailable at the times of the experiments. The trajectory of the BeCu foils was measured using side-on radiography. From 2D simulations of these foils streak camera radiographs have been synthesized. These were used to deduce from the simulations the apparent position of the back of the foil, defined as the point of 50% transmission of the backlighter. In Fig. 3 the simulated trajectory is compared with the simulated position for a flat foil of the same minimum thickness. The trajectories are seen to diverge at $\sim 4 \text{ ns}$, with the perturbed foil moving faster. At this time the RT bubble has penetrated the entire foil; that is the foil has burned through. As the bubble begins to burn through the foil the ablation pressure accelerates a relatively smaller payload, resulting in higher acceleration. Therefore accurate simulation of the side on measurement requires that the foil perturbation be included.

Figure 4 compares the experimental data from two shots with the position obtained from the 2D simulation using the nominal drive model with QEOS and OPAL/STA opacities. There is good agreement between the simulated and measured foil trajectories following shock breakout at $\sim 2.4 \text{ ns}$.

The simulated position obtained with the drive scaled from the photoconducting diode arrays produces very similar results; it matches the position from the nominal drive through 3.8 ns . After that time it is slightly slower, lagging by $12 \mu\text{m}$ at 5.0 ns .

The x-ray flux histories implied by the Dante, photoconducting diode array, witness plate and side on imaging measurements for two different foil materials are in reasonable agreement. There is some variation in measured laser power between shots. Accordingly the radiation flux was adjusted in proportion to laser power, with an allowance for variation in albedo with temperature, during most of the laser pulse duration. After 1.8 ns , when the laser power drops, the radiation

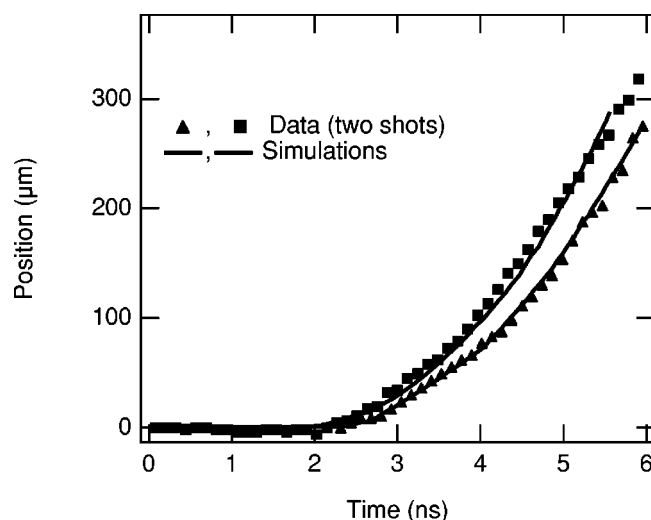


FIG. 4. Symbols indicate position of back of foil deduced from streaked radiographs. Positions taken of back of foil, from 50% intensity point of simulated radiographs, are shown as solid curves

flux is instead adjusted in proportion to the cumulative energy deposited.

The simulated foil trajectory exhibits a small degree of sensitivity to the choice of EOS and opacity models. When the scaled Be EOS table is used instead of QEOS the foil trajectory is slightly slower than the data. Simulations with QEOS are found to be a slightly better fit to the experimental measurements of foil trajectory. The positions obtained with the different opacity models do not differ enough to select among them from the side on measurement.

B. Face on experiments

Data has been obtained from face on experiments for foils having perturbations with $[\lambda = 30 \mu\text{m}, \eta_0 = 1 \mu\text{m}]$, $[\lambda = 50 \mu\text{m}, \eta_0 = 2 \mu\text{m}]$, and $[\lambda = 70 \mu\text{m}, \eta_0 = 2 \mu\text{m}]$. The perturbations on these foils grow in several stages. Prior to shock breakout $\sim 2.2 \text{ ns}$ the propagation of the rippled shock dominates the evolution. Since $a_0/\lambda \sim 0.03\text{--}0.04$ for these foils, the perturbations undergo a brief period of linear regime RT exponential growth following shock breakout. The perturbations subsequently evolve into the nonlinear regime, marked by the appearance of a second harmonic, where saturation results in linear growth versus time. This is followed by burn through, where the observed optical depth modulation rolls over.

The rollover of the Fourier components of optical depth modulation is partly an instrumental artifact as the mass is concentrated into narrow spikes. Since the spikes are highly elongated, experimentally deduced Fourier mode amplitudes during the burn through phase are more sensitive to the instrumental resolution as well as any misalignment of the spikes with the imaging axis. At this late time the Lasnex mesh is highly distorted. Modeling of the foil burn through may be inexact and is not the focus of this work. Shell burn through is not a feature of a successful capsule design.

The shock transit and linear RT growth phases present the most sensitive tests of modeling. The sensitivity of the

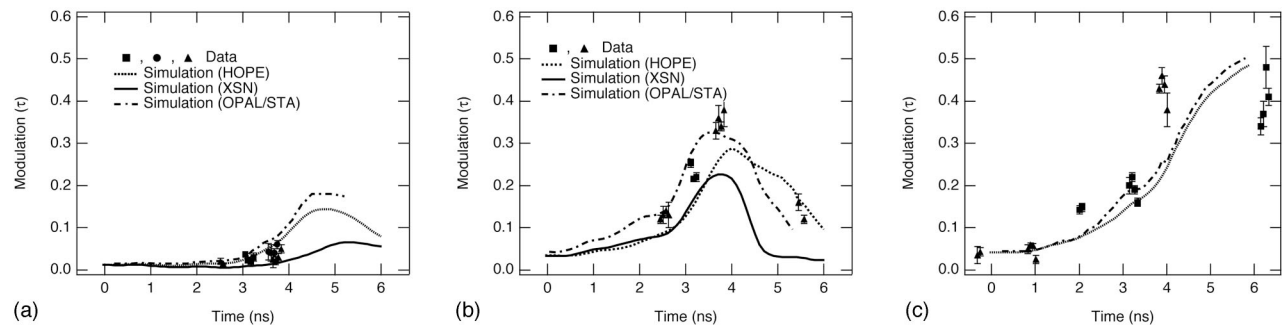


FIG. 5. Symbols indicate measured time evolution of fundamental Fourier mode of optical depth modulation. Wavelengths of perturbations in (a)–(c) are $\lambda = 30, 50$, and $70 \mu\text{m}$, respectively. Curves show simulated fundamental mode amplitude of three opacity models, XSN, HOPE, and composite OPAL/STA.

amplitudes to the linear regime growth rates is greater. And these linear regime growth rates are more sensitive to variations in preheat and ablation front characteristics.

Figures 5(a)–5(c) compare the fundamental Fourier mode amplitude of the perturbation from experiment with simulations performed with the various opacity models. In Figs. 6(a) and 6(b) the comparison for the second harmonic amplitude is shown. Due to the low instrumental resolution at $\lambda = 30 \mu\text{m}$ the observed amplitude is reduced and no second harmonic is observed.

As seen in Figs. 5 and 6, the simulations performed with the XSN opacities predicted somewhat less growth and earlier burn through than measured. Simulations performed with the HOPE opacity tables showed improved agreement with the data. Simulations performed using the composite OPAL/STA opacity tables agree well with the fundamental mode amplitudes. The second harmonic amplitude is also in reasonably good agreement. With the latter opacity model simulated peak fundamental mode growth factors for the foils are 13.4 for $\lambda = 30 \mu\text{m}$, 8.2–8.5 for $\lambda = 50 \mu\text{m}$ and 12.6 for $\lambda = 70 \mu\text{m}$.

The differences in the optical depth modulation obtained from simulations with different opacity models are primarily due to differences in the perturbation growth. The variations in the opacities to backlighter x rays have a smaller impact, increasing the contrast by about 10% for OPAL/STA compared to XSN for the rhodium backlighter.

Figure 7 compares opacities for the three models for representative conditions of the ablation front, $\rho = 0.4 \text{ g/cm}^3$, $T_e = 100 \text{ eV}$. The OPAL/STA composite opacity is higher than XSN below the copper m edge at $h\nu$

$= 0.15 \text{ keV}$ and around the copper l edges near 1 keV . Since the OPAL/STA composite opacities are more opaque to the drive spectrum, they put the foil on a lower adiabat and also reduce the density gradient scale length in the ablator. In addition to the higher RT growth rate the simulation with OPAL/STA opacities saturate at higher levels because lower x-ray preheat causes the foil to decompress more slowly.

When one compares the opacities for each element separately, the differences between XSN and the detailed models is larger for the copper than for the beryllium. Thus for the NIF ignition design, which has a lower copper concentration than the foils used in these experiments, the differences between the ablation front characteristics obtained with the two models is diminished. Simulations with 0.9% Cu concentration show only a slight steepening of the density gradient and a reduction in the rate of ablation for the OPAL/STA opacities compared with XSN. For the BeCu capsule design, the most significant difference resulting from the opacity models is in the ablation rate. Since most of the ablator burns off during the implosion, the modest differences in ablation rate result in relatively larger differences in the ablator mass at ignition. This can affect the tamping of the fuel. In 1D simulations of the 300 eV capsule design⁸ however the yield changed less than 1% between the two ablator opacity models.

The temporal history of the radiation flux in our model is well constrained by the measurements described earlier. Since the shape of the drive spectrum is less tightly constrained we examined its influence on the results. Most of the departure from a Planckian arises from x rays emitted by

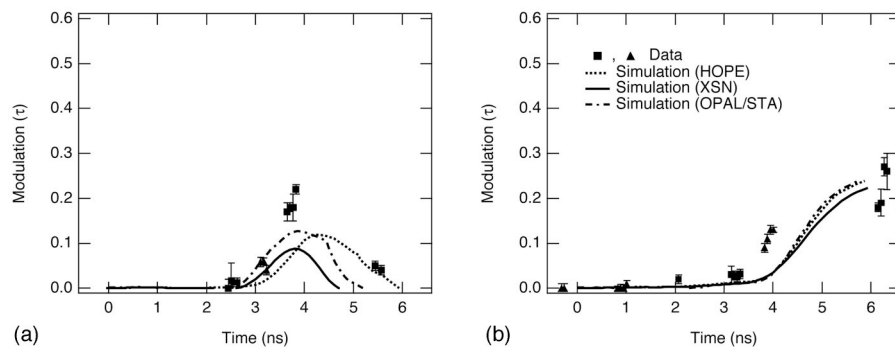


FIG. 6. Symbols indicate measured time evolution of second harmonic Fourier mode of optical depth modulation for foils having $\lambda = 50, 70 \mu\text{m}$ in (a) and (b), respectively. These are compared with results of simulations run with three opacity models.

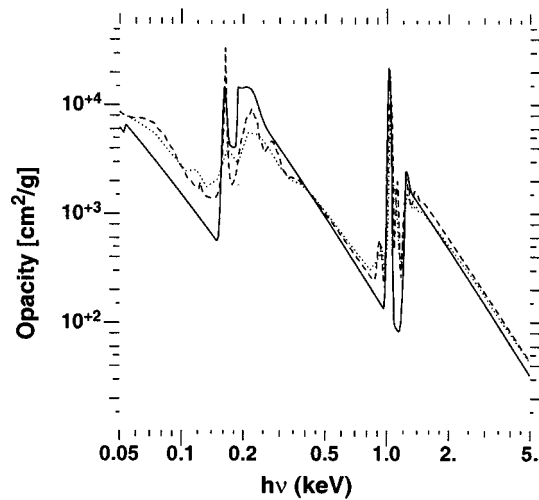


FIG. 7. BeCu opacities for conditions of 0.4 g/cm^3 , $T_e = 100 \text{ eV}$. Solid curve is XSN, dotted curve is HOPE, and dashed curve is from composite OPAL/STA table.

spots on the wall illuminated directly by the laser. The drive spectrum affects the RT in two ways. The hard x-rays deposit much deeper in the foil than the ablation front, where the bulk of the drive deposits, lowering the density of the unablated material. The shape of the drive spectrum in the band carrying most of the flux also affects the shape of the density profile in the ablation front, since photons of different frequencies penetrate to different lengths.¹⁶ To examine the sensitivity of the perturbation growth to the source spectrum shape the calculation was repeated with a $3\times$ preheat enhancement of the spectrum applied for all times above $h\nu = 1.5 \text{ keV}$, where the gold M -band contribution is prevalent. The total area under the spectrum was renormalized to maintain the same source temperature. We also repeated the simulation with a Planckian source spectrum. The spectrum with the $3\times$ enhancement for all time and Planckian spectrum represent implausible extremes, but conveniently illustrate the sensitivity of the perturbation growth to the spectrum shape.

These changes in the spectrum have essentially no effect on the foil position for a simulation of a flat foil. Instead the spectrum affects the perturbation growth. Figure 8 illustrates the effects on fundamental mode growth for the $\lambda = 50 \mu\text{m}$ perturbation. With the enhanced preheat component the perturbation grew somewhat slower, peaking at a value just $\sim 6\%$ less, 400 ps later than for the nominal spectrum. For the Planckian the peak value is 10% higher than for the nominal spectrum. Much of the difference in perturbation growth results from the effect of varying levels of preheat on the rippled shock propagation through the foil. X-ray preheat of material before it has been shocked has more effect than deposition of the same amount of energy after the shock has passed through.¹⁶

Figure 9 shows the sensitivity to the EOS modeling. Results with a Be table from the tabular EOS data base are compared with those obtained with QEOS. The lookup routine applies Thomas–Fermi scaling of the table EOS values to account for the addition of the Cu dopant. The differences

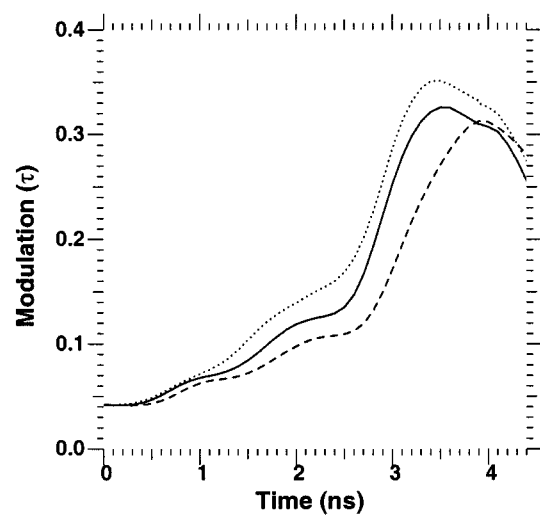


FIG. 8. A comparison of fundamental mode growth in contrast for $\lambda = 50 \mu\text{m}$ wavelength, $\eta_0 = 2 \mu\text{m}$ imposed perturbation from simulations using different drive spectra. Solid curve was obtained with nominal spectrum. Dashed curve is with $3\times$ preheat enhancement above 1.5 keV for all time. Dotted curve is with a Planckian drive spectrum.

due to the EOS models show up primarily during the shock transit phase, prior to 2.4 ns. The important EOS difference is in the foil compression. The table gives higher compression following the shock than does QEOS. The calculated value of density ratio ρ_U/ρ_D for the first shock (at 1.0 ns) is 0.38 for the table compared with 0.47 for QEOS. Larger compression (smaller ρ_U/ρ_D) for the table results in higher growth for the rippled perturbation. This is because the transverse fluid velocity following the shock is proportional to the fluid velocity difference across the shock, which increases with compression.¹⁶ The transverse flow behind the rippled shock carries material from the bubble to the spike. The RT perturbation growth rate during the foil acceleration is nearly the same for the two EOS models. The overall

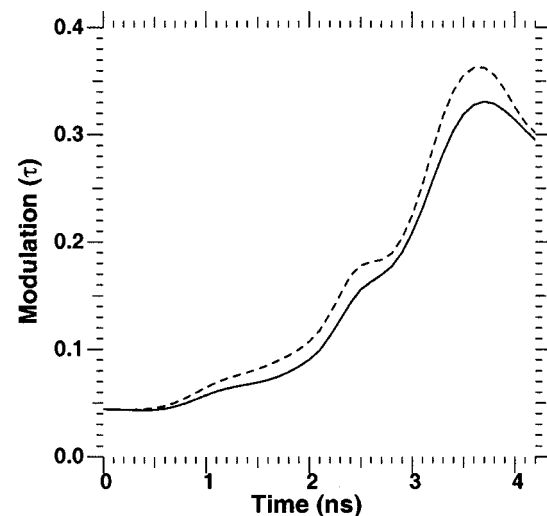


FIG. 9. Sensitivity of perturbation growth to the EOS modeling. Fundamental mode growth in contrast vs time for $50 \mu\text{m}$, $\eta_0 = 2 \mu\text{m}$ imposed perturbation. Solid curve shows results for QEOS; dashed curve is with tabular EOS. All simulations shown employ composite OPAL/STA opacity tables.

differences in growth factor are of order 10%. The comparison between simulations and measurement for the full data set shows the simulations with QEOS are a slightly better match.

For completeness we compare conditions in the ablation front of these beryllium foils with the brominated polystyrene foils reported in previous studies.^{13–18} A CH(Br) foil [$C_{50}H_{47}Br_{2.7}$] 78 μm thick was simulated using the same drive as for a 51 μm thick beryllium copper foil. The greater thickness was chosen for the lower density plastic, nearly to match the ablation front accelerations for 0.7 ns following shock breakout. During this period the average ablation velocity ($V_a \equiv \dot{m}/\rho_a$) was 30% larger in the beryllium. The density gradient scale length [$L_\rho \equiv (d \ln \rho / dz)^{-1}$] had an average value 25% larger in the beryllium. Both of these values vary with time as the foils decompress. For conditions at breakout an estimate of the relative growth rates can be made with the familiar Takabe–Lindl-type formula^{29–31}

$$\gamma = \sqrt{\frac{kg}{(1 + kL_\rho)}} - \beta k V_a,$$

where k is the wave number, and g is the interface acceleration. If we take $\beta = 2$ and use a representative acceleration of 22 $\mu\text{m}/\text{ns}^2$, the estimated ratios of beryllium to plastic growth rates for 30, 50, and 70 μm wavelengths are 0.71, 0.83, and 0.87, respectively. As discussed earlier, the growth rates realized in a given foil will depend upon drive spectrum, foil adiabat and acceleration profile.

III. CONCLUSIONS

Our simulations of the copper-doped beryllium ablator experiments, which make use of the best first principles physical ingredients available to us, agree well with measured RT modulation growth and foil trajectory. The ingredients included opacities calculated by detailed atomic physics modes, HOPE, OPAL, and STA, and the analytic EOS model QEOS. Of all ingredients used in the modeling, the opacities had by far the largest effect on the results when varied within their ranges of uncertainty. The composite opacities obtained for the mixture from OPAL for beryllium and STA for copper produced the most accurate fit to the data. The OPAL/STA model gave higher opacities in specific frequency bands than the XSN model, placing the foil on a lower adiabat and decreasing the ablator density gradient scale length, resulting in higher growth of instabilities. For the NIF ignition design, which has a lower copper concentration than the foils used in these experiments, the differences between the ablation front characteristics obtained with the two models is diminished.

The instability growth exhibited relatively modest sensitivity to the drive spectrum shape. We employed a drive history obtained from hohlraum simulations, adjusted to match temperature measured with Dante, corrected for the wall albedo. The drive model fits the Dante and witness plate data, as well as foil acceleration data for two foil materials.

ACKNOWLEDGMENTS

We thank E. de Prandières for helpful discussions regarding data analysis techniques.

This work was performed under the auspices of the U.S. Department of Energy by the University of California Lawrence Livermore National Laboratory under Contract No. W-7405-Eng-48.

- ¹J. D. Lindl, *Phys. Plasmas* **2**, 3933 (1995).
- ²S. W. Haan, S. M. Pollaine, J. D. Lindl, L. J. Suter, R. L. Berger, L. V. Powers, W. E. Alley, P. A. Amendt, J. A. Futterman, W. K. Levedahl, M. D. Rosen, D. P. Rowley, R. A. Sacks, A. I. Shestakov, G. L. Strobel, M. Tabak, D. B. Harris, N. M. Hoffman, and B. H. Wilde, *Phys. Plasmas* **2**, 2480 (1995).
- ³W. J. Krauser, N. M. Hoffman, D. C. Wilson, B. H. Wilde, W. S. Varnum, D. B. Harris, F. J. Swenson, P. A. Bradley, S. W. Haan, S. M. Pollaine, A. S. Wan, J. C. Moreno, and P. A. Amendt, *Phys. Plasmas* **3**, 2084 (1996).
- ⁴T. R. Dittrich, S. W. Haan, S. Pollaine, A. K. Burnham, and G. L. Strobel, *Fusion Technol.* **31**, 402 (1997).
- ⁵T. R. Dittrich, S. W. Haan, M. M. Marinak, S. M. Pollaine, and R. McEachern, *Phys. Plasmas* **5**, 3708 (1998).
- ⁶T. R. Dittrich, S. W. Haan, M. M. Marinak, S. M. Pollaine, D. E. Hinkel, D. H. Munro, C. P. Verdon, G. L. Strobel, R. McEachern, R. C. Cook, C. C. Roberts, D. C. Wilson, P. A. Bradley, L. R. Foreman, and W. S. Varnum, *Phys. Plasmas* **6**, 2164 (1999).
- ⁷D. C. Wilson, P. A. Bradley, N. M. Hoffman, F. J. Swenson, D. P. Smitherman, R. E. Chrien, R. W. Margevicius, D. J. Thoma, L. R. Foreman, J. K. Hoffer, S. R. Goldman, S. E. Caldwell, T. R. Dittrich, S. W. Haan, M. M. Marinak, S. M. Pollaine, and J. J. Sanchez, *Phys. Plasmas* **5**, 1953 (1998).
- ⁸M. M. Marinak, S. W. Haan, T. R. Dittrich, R. E. Tipton, and G. B. Zimmerman, *Phys. Plasmas* **5**, 1125 (1998).
- ⁹J. A. Paisner, J. D. Boyes, S. A. Kumpan, W. H. Lowdermilk, and M. S. Sorem, *Laser Focus World* **30**, 75 (1994).
- ¹⁰R. McEachern, C. Alford, R. Cook, D. Makowiecki, and R. Wallace, *Fusion Technol.* **31**, 435 (1997).
- ¹¹R. W. Margevicius, L. J. Salzer, M. A. Salazar, and L. R. Foreman, *Fusion Technol.* **35**, 106 (1999).
- ¹²K. V. Salazar, S. G. Patillo, and M. Trkula, *Fusion Technol.* **38**, 69 (2000).
- ¹³B. A. Remington, S. W. Haan, S. G. Glendinning, J. D. Kilkenny, D. H. Munro, and R. Wallace, *Phys. Fluids B* **4**, 967 (1992).
- ¹⁴B. A. Remington, S. V. Weber, S. W. Haan, J. D. Kilkenny, S. G. Glendinning, and R. J. Wallace, *Phys. Fluids B* **5**, 2589 (1993).
- ¹⁵B. A. Remington, S. V. Weber, M. M. Marinak, S. W. Haan, J. D. Kilkenny, R. J. Wallace, and G. Dimonte, *Phys. Plasmas* **2**, 241 (1995).
- ¹⁶S. V. Weber, B. A. Remington, S. W. Haan, B. G. Wilson, and J. K. Nash, *Phys. Plasmas* **1**, 3652 (1994).
- ¹⁷M. M. Marinak, B. A. Remington, S. V. Weber, R. E. Tipton, S. W. Haan, K. S. Budil, O. L. Landen, J. D. Kilkenny, and R. Wallace, *Phys. Rev. Lett.* **75**, 3677 (1995).
- ¹⁸M. M. Marinak, S. G. Glendinning, R. J. Wallace, B. A. Remington, K. S. Budil, S. W. Haan, R. E. Tipton, and J. D. Kilkenny, *Phys. Rev. Lett.* **80**, 4426 (1998).
- ¹⁹J. D. Kilkenny, *Rev. Sci. Instrum.* **63**, 4688 (1992).
- ²⁰K. S. Budil, T. S. Perry, P. M. Bell, J. D. Hares, P. L. Miller, T. A. Peyser, R. Wallace, H. Louis, and D. E. Smith, *Rev. Sci. Instrum.* **67**, 485 (1996).
- ²¹E. M. Campbell, *Laser Part. Beams* **9**, 209 (1991).
- ²²G. B. Zimmerman and W. L. Krue, *Comments Plasma Phys. Controlled Fusion* **2**, 51 (1975).
- ²³R. L. Kauffman, L. J. Suter, C. B. Darrow *et al.*, *Phys. Rev. Lett.* **73**, 2320 (1994).
- ²⁴G. B. Zimmerman and R. M. More, *J. Quant. Spectrosc. Radiat. Transf.* **23**, 517 (1980); R. M. More, *ibid.* **27**, 345 (1982).
- ²⁵B. F. Roznyai and M. Lamoureux, *J. Quant. Spectrosc. Radiat. Transf.* **43**, 381 (1990).
- ²⁶C. A. Iglesias, F. J. Rogers, and B. G. Wilson, *Astrophys. J.* **397**, 717 (1992); **360**, 221 (1990); *Astrophys. J. Lett.* **322**, L45 (1987); F. J. Rogers and C. A. Iglesias, *Astrophys. J., Suppl.* **79**, 507 (1992).
- ²⁷A. Bar-Shalom, J. Oreg, W. H. Goldstein, D. Shvarts, and A. Zigler, *Phys. Rev. A* **40**, 3183 (1989).
- ²⁸R. M. More, K. H. Warren, D. A. Young, and G. B. Zimmerman, *Phys. Fluids* **31**, 3059 (1988).
- ²⁹H. Takabe, L. Montierth, and R. L. Morse, *Phys. Fluids* **26**, 2299 (1983).
- ³⁰M. Tabak, D. H. Munro, and J. D. Lindl, *Phys. Fluids B* **2**, 1007 (1990).
- ³¹R. Betti, V. N. Goncharov, R. L. McCrory, and C. P. Verdon, *Phys. Plasmas* **5**, 1446 (1998).